



Original Research Article

Aerodynamic Performance of the NACA 63-012 Airfoil with Sinusoidal-Shaped Leading Edge at Low Air Velocity

¹Kunya, B.I., ^{*2}Aliyu, A.B. and ²Salihu, B.M.

¹Department of Mechanical Engineering, Faculty of Engineering, Kano University of Science and Technology, Wudil, PMB 3244, Kano, Nigeria.

²Department of Mechanical Engineering, Federal Polytechnic Mubi, Adamawa State, Nigeria.

*adamuldam@yahoo.com; kunyabashir@yahoo.com

ARTICLE INFORMATION

Article history:

Received 26 Aug, 2020

Revised 17 Oct, 2020

Accepted 29 Oct, 2020

Available online 30 Dec, 2020

Keywords:

Angle of attack

Lift coefficient

Drag coefficient

Bumps

Flow separation

ABSTRACT

This research work focused on numerical simulation of the effect of sinusoidal bumps (or tubercles) at the leading edge of an airfoil on efficiency using NACA 63-012 cross-section profiles. Two computational softwares (GAMBIT and FLUENT) were used. The GAMBIT was used for the modeling and meshing while the FLUENT was used for the simulation. Shear stress transport (k - ω or k - ω) and Spalart Allmaras (SA) turbulence models available in the simulation software were used. The characteristics investigated included flow separation (or stall), lift and drag, angle of attack, and bumps effect at low Reynolds number. The results show that bumps on the blade leading edge have advantage at higher angle of attack for both turbulence models.

© 2020 RJEES. All rights reserved.

1. INTRODUCTION

Aerodynamics is the study of the dynamics (motion) of air (or gases), or the interaction between moving object and atmosphere causing an airflow around a body. It is a sub-field of fluid dynamics, and many aspects of aerodynamics theory are common to these fields. Understanding the motion of air around an object (often called a flow field) enables the calculation of forces and moments acting on the object. The forces of interest in many aerodynamics problems are the fundamental forces of flight i.e., lift, drag, thrust, and weight. Of these, lift and drag are aerodynamics forces, i.e., forces due to air flow over a solid body (Douglas et al., 2005). The use of aerodynamics through mathematical analysis, empirical approximations, wind tunnel experimentation, and computer simulations has formed a rational basis for the development of heavier-than-air flight and a number of other aerodynamic technologies.

An airfoil is a stream line body, i.e., it has a rounded leading edge, is elongated and is given a gradual curvature in the flow direction. The airfoil sections employed for airplane wings, propellers, wind turbine, etc. are of such a geometrical configuration as to produce high lifts and low drag values. The lift on an airfoil

is primarily the result of its angle of attack and shape (Douglas et al., 2005). When oriented at a suitable angle, the airfoil deflects the oncoming air, resulting in a force on the airfoil in the direction opposite to the deflection. Airfoils mostly look different from one another and designers have not settled on a common design because, the flow conditions and design goals change from one application to the next (Isyaku, 2019).

The main approach to improving the performance of airfoil especially at low wind speeds is to maximize the lift force by increasing its angle of attack with the incoming air. A recurring problem is that increasing the angle of attack eventually causes stalling (Thumthae and Chitsomboon, 2009). If a technology could be developed to boost the operating angle of the airfoil, the prospect exists for improvement of its performance.

Mimicking the geometrical nature of the flippers of humpback whales may provide the solution for improving performance of airfoil. The humpback whale (*Megaptera novaeangliae*) is a species of the largest group of baleen whale. The humpback has a distinct body shape, with long pectoral flippers (fins) and a knobby head. It is known for breaching, tail-lobbing and pectoral fin slapping as the common surface behavior. The flippers have a series of sinusoidal-shaped bumps called tubercles on their leading edge (Fish and Battle, 1995).

According to some computational and experimental research works conducted, introduction of tubercles (bumps) on airfoil leading edge can impact the airfoil performance the same way it does for humpback whale. To cite examples, Hansen *et al.* (2011) studied experimentally the influence of bump height, and sinusoidal wavelength at the leading edge of NASA 65-021 and NASA 0021 foils. The results show that the tubercle leading edge was more beneficial for the NASA 65-021 foil than for the NASA 0021 foil and that both tubercle foils showed increased maximum lift coefficient and a larger stall angle than the conventional foil. Gawad (2012) carried out a numerical simulation of the effect of tubercles on the flow characteristics around NASA 0012 airfoil and found that tubercles delayed stall at a higher angle of attack, and the maximum value of lift coefficient and the angle at which stall occurs increases with Reynolds number for both the regular and tubercle airfoils. The values of the drag coefficient of tubercle airfoil are greater than those of regular airfoil. The results of the computational investigation of the effect of protuberances at the leading edge of a thick airfoil (S809) by Asli *et al.* (2015) at 10^6 Reynolds number revealed that, at low angles of attack before the stall region, lift coefficient decreased slightly rather than the baseline model. However, the modified airfoil has a smooth stall trend while the baseline airfoil lift coefficient sharply reduced due to the separation which occurred on a suction side. Kunya *et al.* (2019) studied numerically and experimentally the effect of varying sinusoidal bumps (or tubercles) height at the leading edge of airfoil on efficiency using NASA LS (1)-0413 cross-section profiles.

The survey of the previous studies revealed that the leading-edge tubercles allow the operation of the airfoil at higher angle of attack before stall (separation) would occur, thus, improving its performance. However, based on the available literature, this is the first time research on the experimental and numerical study of the effect of sinusoidal bumps at the leading edge of airfoil with NACA 63-012 cross-section profile at low Reynolds Number (in the order of 10^4) was conducted. Most studies were done at relatively higher Reynolds number (in the order of 10^5 and above) and used different airfoil sections. This arise the need for this research which ascertained that the innovation (of introducing airfoil leading edge bumps) is applicable.

This study is thus limited to computational study of the effect of sinusoidal bumps on the leading edge of airfoil based on NACA 63-012 cross-section profiles at low Reynolds number (that is, 41075.22 based on 6 m/s air velocity and 0.1 m airfoil chord length).

2. METHODOLOGY

The study involved the use of computational fluid dynamic (CFD) method on the airfoil with NACA 63-012 cross-section using Shear stress transport k-omega and Spalart Allmaras turbulence models.

2.1. The NACA 63-012 Airfoil

The NACA 63-012 is the family of the NACA six series family. The first digit (6) denotes the series and indicates that this family is designed for greater laminar flow than the Four- or Five-Digit Series. The second digit, 3, is the location of the minimum pressure in tenths of chord (0.3c). The final two digits specify the thickness in percentage of chord (12%). Table 1 shows the co-ordinates of the NACA 63-012 airfoil section (Dylan Walsh (10320467) Energy Systems Engineering, 2013).

Table 1: Coordinates of the NACA 63-012 airfoil section in percent of airfoil chord

Upper surface		Lower surface	
Station	Ordinate	Station	Ordinate
0.0	0.0	0.0	0.0
0.5	0.9837	0.5	-0.9837
0.75	1.1938	0.75	-1.1938
1.25	1.5181	1.25	-1.5181
2.5	2.0980	2.5	-2.0980
5	2.9256	5	-2.9256
7.5	3.5432	7.5	-3.5432
10	4.0386	10	-4.0386
15	4.8003	15	-4.8003
20	5.3431	20	-5.3431
25	5.7115	25	-5.7115
30	5.9304	30	-5.9304
35	6.0005	35	-6.0005
40	5.9220	40	-5.9220
45	5.7051	45	-5.7051
50	5.3698	50	-5.3698
55	4.9354	55	-4.9354
60	4.4206	60	-4.4206
65	3.8398	65	-3.8398
70	3.2113	70	-3.2113
75	2.5567	75	-2.5567
80	1.9002	80	-1.9002
85	1.2724	85	-1.2724
90	0.7076	90	-0.7076
95	0.2521	95	-0.2521
100	0.0000	100	-0.0000

L.E. radius: 1.004 percent chord

2.2. Specifying the Bumps Geometry on the Blade Leading Edge

It was mentioned earlier that bumps on turbine blade leading edge improve its performance by delaying flow separation at higher angle of attack. However, there is not yet a fixed geometry of the bumps believed to give a better performance of the turbine blades. Therefore, bumps design can be an iterative process as there is no any geometrical relationship known for their design. For this study, bumps with sinusoidal shape, 6% chord length amplitude (as approximately there on the natural whale pectoral fins), and inter-tubercular distance of 20% span was used for the selected NACA airfoil section using CAD software (GAMBIT).

2.3. Creating the Models and the Flow Domain

The models and the C-grid domain were created in GAMBIT modeling software. The steps followed during the process are:

1. Imported the airfoil coordinate as obtained into GAMBIT
2. Modified the airfoil coordinate within GAMBIT into a three-dimensional model
3. Created the C-grid
4. Connected the C-grid and the airfoil using GAMBIT's edge and face command.
5. Created the volumes that describe the entire geometry.

2.3.1. Obtaining and importing the airfoil coordinates

The airfoil coordinates for the NACA 63-012 were obtained as developed by the National Advisory Committee for Aeronautics (NACA). The coordinates (in text document type format) were imported into GAMBIT and appear as shown by Figure 1.

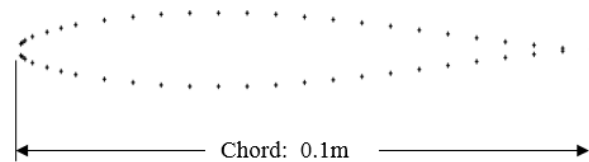


Figure 1: NACA 63-012 coordinate representation in GAMBIT

2.3.2. Modifying the airfoil coordinate into a three-dimensional model

To create the three-dimensional model of the conventional airfoil, two edges were created for the upper and lower coordinates points. This makes a face bounded by these edges. The edges were swept (or extruded) along the z-axis to a depth of 0.15 m span to create faces, and then the three-dimensional airfoil. Now, the three-dimensional airfoil includes exactly six edges and four faces. For the bumpy airfoil, the leading edge was replaced by a sinusoidal edge before creating faces by importing the bumps coordinates and using Nurbs line function in the GAMBIT. The airfoils created are shown by Figures 2 and 3.

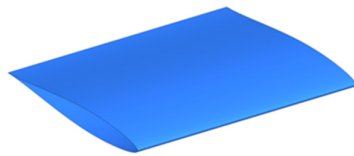


Figure 2: Conventional leading-edge airfoil

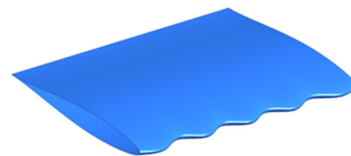


Figure 3: Bumpy airfoil

2.3.3. Creating the C-grid

The C-grid was created in GAMBIT using geometry controls with a distance of 20 times airfoil chord length ($20c$) upstream of leading edge, $20c$ downstream of the trailing edge and a height of $20c$ for the upper and lower domain. The airfoils chord length (c) is 0.1 m. The result is shown by Figure 4. The C-grid was extruded along the z-axis to a depth equal to that of the airfoil span as shown in Figure 5.

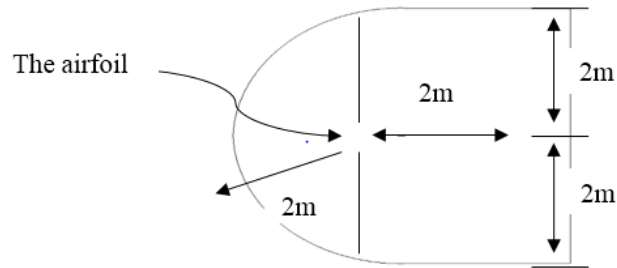


Figure 4: The C-grid

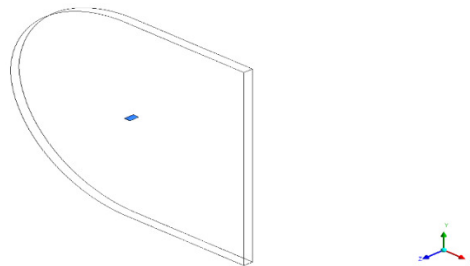


Figure 5: Three-dimensional C-grid with airfoil highlighted in blue

2.3.4. Connecting the C-grid and the airfoil

The C-grid structure was decomposed into four regions using GAMBIT's edge and face command. These regions enabled structured meshing schemes used in the geometry as shown in Figure 6.

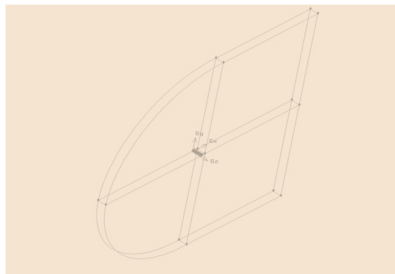


Figure 6: Connected C-grid and airfoil (showing four distinct regions)

2.3.5. Creating volumes in the domain

Each of the four distinct regions was converted into volume using GAMBIT's volume commands, which were then meshed individually. This method makes it easier to control the structured mesh, cell sizes, boundary layer and element (cell) number.

2.4. Mesh Generation

The four volumes created within the computational domain were meshed. The following steps were followed.

1. Determined the airfoil's boundary layer requirements
2. Mesh the entire volume using the boundary layer requirements.

3. Defined the boundary type on the volume faces
4. Exported the mesh into FLUENT.

2.4.1. Airfoil's boundary layer requirements (Y and Y+)

A Y^+ value of 1 was used in determining the grid spacing at the boundary layer for all airfoils in this simulation as this will resolve the boundary layer accurately. Using a Y^+ value of 1 and a chord length of 0.1m the Y normal wall distance was calculated approximately as $4.1e-5m$ or $0.000041m$. Figure 7 shows how the mesh is affected by the first cell grid spacing ($Y = 4.1e-5m$) and the subsequent cell geometric expansion of 1.2.

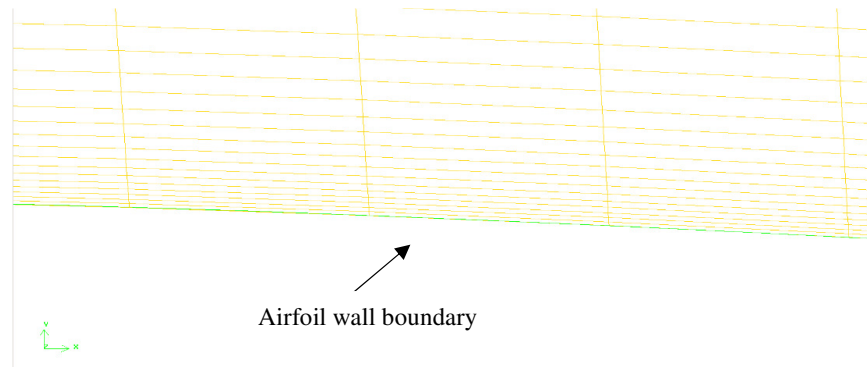


Figure 7: Mesh around the airfoil wall

2.4.2. Meshing the entire volume

All the faces of the domain sub-volumes were meshed by using the nodes created on their edges. Each region of the volumes was then meshed with a structured scheme; the entire cells are hexahedral with 875000 cells in total for all models. Figure 8 shows the mesh for the entire domain.

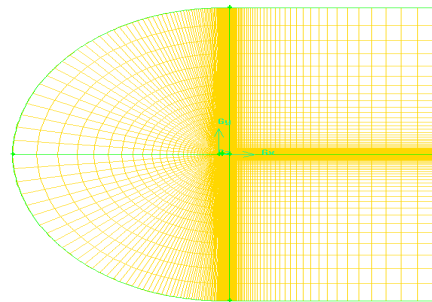


Figure 8: The entire mesh

2.4.3. Defining the boundary type on the volume faces

The faces that made up the boundary of the computational domain are defined before exporting the mesh to FLUENT. These boundary types are the airfoil wall, the inlet, the outlet, and the symmetry boundaries. The file was exported into FLUENT as an msh file and set-up the simulation.

2.5. Governing Fluid Dynamic Equations

Fluid dynamics is the study of fluid motion that involves forces of action and reaction, i.e. forces which cause acceleration and forces which resist acceleration. The equations governing the fluid motion are the three fundamentals principles of mass, momentum, and energy conservation. These are (Nasser and Javad, 2012):

$$\text{Continuity equation:} \quad \frac{\partial \rho}{\partial t} + \nabla \cdot (\rho V) = 0 \quad (1)$$

$$\text{Momentum equation:} \quad \rho \frac{\partial V}{\partial t} + V \cdot \nabla (\rho V) = \nabla \cdot \tau_{ij} - \nabla P + \rho F \quad (2)$$

$$\text{Energy equation:} \quad \rho \frac{De}{Dt} + P(\nabla \cdot V) = \frac{\partial Q}{\partial t} - \nabla \cdot q + \Phi \quad (3)$$

One or more terms might be neglected depending on the nature of physics governing the fluid motion. If the flow is incompressible, for example, and the coefficient of viscosity of the fluid, (μ), as well as coefficient of thermal conductivity are constant, the continuity, momentum, and energy equations reduce to the following equations (Nasser and Javad, 2012):

$$\nabla \cdot V = 0 \quad (4)$$

$$\rho \frac{\partial V}{\partial t} + \rho V \cdot \nabla V = \mu \nabla^2 V - \nabla P + \rho F \quad (5)$$

$$\rho \frac{De}{Dt} = \frac{\partial Q}{\partial t} + k \nabla^2 T + \Phi \quad (6)$$

The presence of each term and their combination determines the appropriate solution algorithm and the numerical procedure.

The Reynolds average Navier-Stokes (RANS) equations are primarily used to describe turbulent flows. These equations can be used with approximations based on knowledge of the properties of flow turbulence to give approximate time averaged solutions to the Navier-Stokes (N-S) equations. Each instantaneous quantity in the N-S equation can be split into time-averaged and fluctuating components, and the resulting equation time averaged, to yield (for incompressible flow) (Nasser and Javad, 2012):

$$\nabla \cdot \bar{V} = 0 \quad (7)$$

$$\frac{\partial \bar{V}}{\partial t} + \bar{V} \cdot \nabla \bar{V} = \frac{\mu}{\rho} \nabla^2 \bar{V} - \frac{1}{\rho} \nabla \cdot \bar{P} + \bar{F} - \overline{\nabla \cdot V^i^2} \quad (8)$$

The non-linear Reynolds stress term $\left(\overline{\nabla \cdot V^i^2} \right)$ requires additional modeling to close the RANS equation for solving and has led to the creation of many different turbulence models.

2.6. Turbulence Models

Spalart Allmaras and shear stress transport turbulence models are used in this research work and are explained in the following sub-headings.

2.6.1. Spalart Allmaras model

Spalart Allmaras is one-equation, low-cost RANS model solving a transport equation for a modified eddy viscosity, $\tilde{\nu}$ (FLUENT 6.3, 2006).

$$\frac{D\tilde{v}}{Dt} = G_v \left\{ \frac{\partial}{\partial y} \left[(\mu + \rho\tilde{v}) \frac{\partial\tilde{v}}{\partial y} \right] + C_{b2}\rho \left(\frac{\partial\tilde{v}}{\partial y} \right)^2 \right\} - Y_v + S_{\tilde{v}} \quad (9)$$

The eddy viscosity is obtained from:

$$\mu_t = \rho\tilde{v}f_{vl} \quad (10)$$

$$f_{vl} = \frac{(\tilde{v}/v)^3}{(\tilde{v}/v)^3 + C_{v1}^3} \quad (11)$$

The variation of \tilde{v} very near the wall is easier to resolve than k and ϵ . The model is designed specifically for aerodynamic or turbo machinery applications with mild separation such as supersonic/transonic flows over airfoils, boundary layer flow, etc. Option to include strain rate in k production term improves predictions of vortical flows.

2.6.2. Standard k - ω model

Standard k - ω model is a two-equation model solving for k and ω , the specific dissipation rate (ϵ/k) based on Wilcox (1998) as cited in FLUENT 6.3 (2006). The model demonstrates superior performance for wall-bounded and low Reynolds number flows. It shows potential for predicting transition. The equations are (FLUENT 6.3, 2006):

$$\mu_t = \alpha^* \rho \frac{k}{\omega} \quad (12)$$

$$\rho \frac{Dk}{Dt} = \tau_{ij} \frac{\partial\bar{u}}{\partial y} - \rho\beta^* f_{\beta^*} k\omega + \frac{\partial}{\partial y} \left[\left(\mu + \frac{\mu_t}{\sigma_k} \right) \frac{\partial k}{\partial y} \right] \quad (13)$$

$$\rho \frac{D\omega}{Dt} = \alpha \frac{\omega}{k} \tau_{ij} \frac{\partial\bar{u}}{\partial y} - \rho\beta^* f_{\beta} \omega^2 + \frac{\partial}{\partial y} \left[\left(\mu + \frac{\mu_t}{\sigma_{\omega}} \right) \frac{\partial \omega}{\partial y} \right] \quad (14)$$

$$\omega \approx \frac{\epsilon}{k} \propto \frac{1}{\tau}$$

2.6.3. Shear stress transport (SST) k - ω model

Shear stress transport (SST) k - ω model is a variant of the standard k - ω model. The model combines the original Wilcox model for use near walls and the standard k - ϵ model away from wall using a blending function. Also limits turbulence viscosity to guarantee that $\tau_t \sim k$. The transition and shearing options are borrowed from standard k - ω . The resulting blended equations are (FLUENT 6.3, 2006):

$$\rho \frac{Dk}{Dt} = \tau_{ij} \frac{\partial\bar{u}}{\partial y} - \rho\beta^* k\omega + \frac{\partial}{\partial y} \left[\left(\mu + \frac{\mu_t}{\sigma_k} \right) \frac{\partial k}{\partial y} \right] \quad (15)$$

$$\rho \frac{D\omega}{Dt} = \frac{\gamma}{v_t} \tau_{ij} \frac{\partial\bar{u}}{\partial y} - \rho\beta^* \omega^2 + \frac{\partial}{\partial y} \left[\left(\mu + \frac{\mu_t}{\sigma_{\omega}} \right) \frac{\partial \omega}{\partial y} \right] + 2\rho(1 - F_1)\sigma_{\omega 2} \frac{1}{\omega} \frac{\partial k}{\partial y} \frac{\partial \omega}{\partial y} \quad (16)$$

$$\phi = F_1\phi_1 + (1 - F_1)\phi_2 \quad ; \quad \phi = \beta, \sigma_k, \sigma_{\omega}, \gamma$$

2.7. Computation and Modeling Software

Two software were used; the GAMBIT (for the modeling and meshing) and FLUENT (for the simulation). GAMBIT is an integrated preprocessor for CFD analysis which can be used to build geometry and generate mesh, or import a geometry created by a third-party CAD package, make modifications, and generate a mesh. GAMBIT meshing options give more flexibility and choices. It is possible to decompose geometries for structured meshing or perform automatic unstructured hexahedral meshing, and to generate high-quality triangular and tetrahedral meshes, as well as meshes containing pyramids and prisms. Gambit is designed for use with a mouse, but most of its operations can also be executed by means of commands entered from the keyboard or from a journal file (GAMBIT 2.3, 2006). FLUENT is a computational fluid dynamics (CFD) software package to simulate fluid flow problems. It uses the finite volume method to solve the governing

equations for a fluid. It provides the capability to use different physical models such as incompressible or compressible, inviscid or viscous, laminar or turbulent, etc (FLUENT 6.3, 2006). Geometry and grid generation is usually done using GAMBIT which is the preprocessor bundled with FLUENT. SST k- ω and SA turbulence models available in FLUENT were used.

2.8. The Flow Solver and Initial Set-up

The pressure-based (segregated and coupled) solver was used to perform the simulations in FLUENT with higher order spatial discretization. The semi-implicit method for pressure linked equations (SIMPLE) algorithm was used for pressure velocity coupling. As suggested by the solver, second-order upwind scheme was implemented for discretizing the equations and second order was used as the pressure interpolation scheme. Default under-relaxation factors provided in the solver were used. Boundary types offer by FLUENT are many; velocity inlet, symmetry, wall, and pressure outlet were used in this study. The flow type is incompressible with a Reynolds number of 41075.22 (this corresponds with 6 m/s inlet velocity and 0.1 m airfoil chord length), a temperature of 300K and a constant air density of 1.225kg/m³ at a pressure of 1 atmosphere. Shear Stress Transport K-Omega and Spalart Allmaras turbulence models were used for the simulation. The turbulent intensity of 1% and turbulent viscosity of 10 were used. The simulation was a steady state pressure-based one and was initially carried out for each turbulent model using segregated solver. Reference values were specified to monitor lift and drag forces and a convergence criterion of 10⁻⁶ is set for the residuals. The convectional NACA 63-012 and 0.06C bumpy NACA 63-012 airfoils were used for the simulations. The angles of attack considered were 0, 5, 10, 15, 20 and 25 degrees.

3. RESULTS AND DISCUSSION

The numerical results obtained from the simulation are presented and discussed in this section. The lift and drag coefficients obtained from the simulations are presented in graphs. The results of the simulation were also viewed by generating contour plots of domain using FLUENT's post processing capabilities.

3.1. Simulations using SA Model: Lift Graphs

Figure 9 shows the variation of lift coefficient with angle of attack for the conventional and bumpy airfoils using Spalart Allmaras turbulence (SA) model.

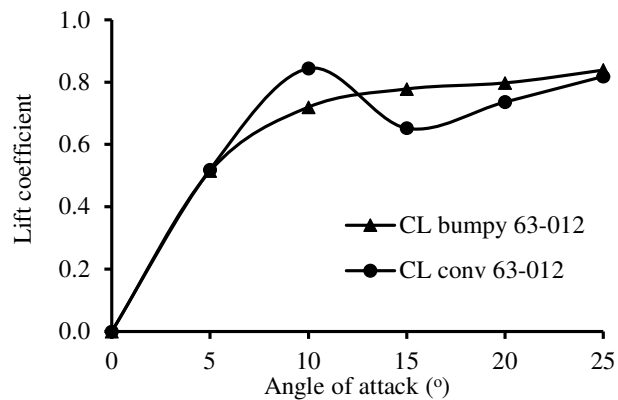


Figure 9: Lift coefficient versus angle of attack using SA model

It can be seen in Figure 9 that, for the convectional airfoil, stall started (that is the point where the lift coefficient just starts to reduce in value) at around 10° angle of attack. The bumpy airfoil had a fairly flat stall regime as its lift curve did not drop but stayed leveled after 10°. The lift curve for the convectional

model achieved a higher maximum lift coefficient than the bumpy airfoil but quickly dropped below that of the bumpy airfoils due to stall effects, only to recover at an angle of 25° . The minimum lift coefficient for the convectional and the bumpy airfoils is 0. The max lift coefficient for the convectional airfoil is 0.84, the bumpy airfoil stayed at a max of 0.8. The point at which the convectional curve dipped below the bumpy curve is between around the angles of 13° and 25° . This result shows that the bumpy airfoil model produced slightly lower lift values in the pre-stall regime above 5° angle of attack, and proved to be more beneficial in the post-stall regime than the conventional one. This is due to the production of stream-wise vortices along the bumpy leading edge. These vortices carried higher momentum flow in the boundary layer, which kept the flow attached to the surface of the airfoil and, in turn, delayed separation, and thus enables a higher lift coefficient during post stall. Previous studies by Anil (2007), Hansen *et al.* (2011), Gawad (2012), and Asli *et al.* (2015) using NACA 2412, NASA 65-021 and NASA 0012, NASA 0012, and S809 (thick) airfoils sections respectively explain similar characteristics even though these studies were conducted at higher Reynolds numbers (in the order of 10^5 to 10^6) than the current research. However, studies by Miklosovic *et al.* (2004) and Carija *et al.* (2014) on airfoil section which resemble NACA six series family, and NACA 0012 respectively obtained similar characteristics but the maximum lift coefficient of conventional airfoil is less than for those with leading edge bumps (i.e., with bumps there were delay of stall); and these researches were also conducted within the same Reynolds number range (10^5) as the previous studies mentioned.

3.2. Simulations using k- ω model: Lift Graphs

Figure 10 shows the variation of lift coefficient with angle of attack for the airfoils using shear stress transport (k- ω) turbulence model. Using the k- ω model, it can be seen in the Figure10 that the convectional airfoil's stall started at 10° angle of attack. The bumpy airfoil had an upward stall regime as its lift curve did not drop but moved up during post stall. The lift curve for the convectional model achieved a higher maximum lift coefficient than the bumpy airfoil but quickly dropped below that of the bumpy airfoil due to stall effects, only to recover at an angle of 25° .

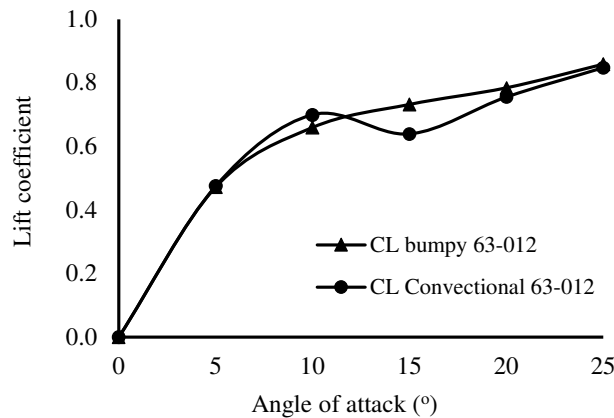


Figure 10: Lift coefficients versus angle of attack using k- ω model

The fact that at stall angle the stream-wise vortices produce by bumps of the bumpy airfoil might not be strong enough to reduce the flow separation with causes lift value drop might be the reason for its lower maximum lift coefficient than the conventional airfoil. However, these vortices are stronger enough to give bumpy airfoil advantage for higher lift value at post-stall than the conventional airfoil. The minimum lift coefficient for the convectional and the bumpy was 0. The maximum lift coefficient (pre stall) for the convectional was 0.7, the bumpy moved up from 0.66 at 10° to 0.73 at 15° . The point at which the convectional curve dipped below the bumpy curve is between the angles of 10 and 15 degrees, approximately at 12° .

Comparison of the two turbulence models (SA and $k-\omega$) graphs (Figures 9 and 10) show similarity in terms of characteristics of lift variation with angle of attack between the conventional and the bumpy airfoils. But, the values of lift coefficient predicted by SA model after 5° angle of attack are greater than those predicted by $k-\omega$ model, for example, the maximum values of lift coefficient for the convectional model using SA and $k-\omega$ models are 0.84 and 0.7 respectively. For the bumpy airfoil, the maximum lift coefficient values are 0.8 and 0.66 respectively for SA and $k-\omega$ models.

3.3. Simulations using SA Model: Drag Graphs

Figure 11 shows the variation of drag coefficient with angle of attack for the airfoils. For both airfoils' graphs in the Figure 11, the drag coefficient value starts to vary almost with the same values (i.e., from 15° angle of attack and above), and show similar characteristics between 0° and 5° angle of attack. From the angle of 0° to 5° , skin friction drag is dominant; hence the drag curve is aligned for both conventional and bumpy (Isyaku, 2019). After 5° angle of attack, flow separation starts for both airfoils and profile drag become dominant, the bumpy airfoil curve deviates from the convectional airfoil; the drag curve for the bumpy airfoil follows a straight line, while the convectional airfoil follows a non-linear curve. This is due to the fact that the leading-edge profiles for the convectional and bumpy airfoils are different (Isyaku, 2019). Both airfoil curves converge at an angle of 15° and they become aligned and move in almost a straight line up to 25° . During the post-stall regime between 15° to 25° angle of attack, the drag coefficients on all models were almost the same; this is because at higher angles, aerofoils (or blades) become bluff bodies such that the bumps have little effect on drag (Isyaku, 2019). Previous studies (Anil, 2007; Hansen *et al.*, 2011; Gawad, 2012; Asli *et al.*, 2015) explain similar lift and drag characteristics between the conventional and bumpy aerofoils even though these studies were conducted at higher Reynolds numbers (in the order of 10^5 to 10^6) than the current research.

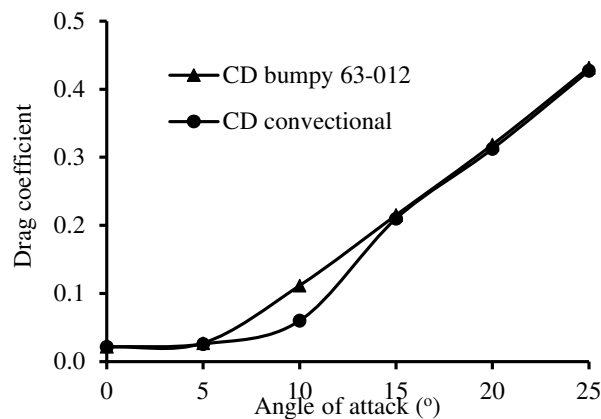
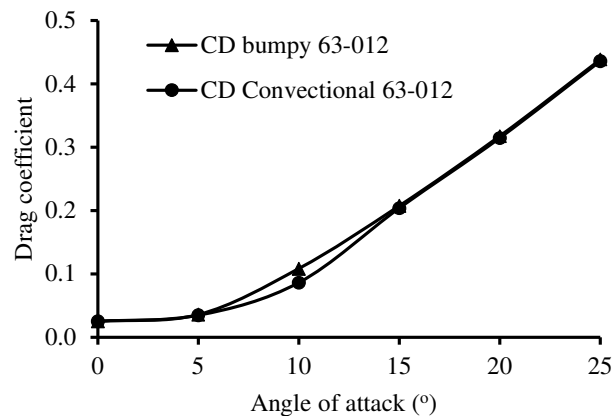


Figure 11: Drag coefficients versus angle of attack using SA model

3.4 Simulations using $k-\omega$ model: Drag Graphs

Figure 12 shows the variation of drag coefficient with angle of attack for the airfoils using shear stress transport ($k-\omega$) turbulence model. A similar pattern was observed in using the $k-\omega$ model as for SA model, but with the non-linearity of the convectional models between 5° and 15° angle of attack not as pronounced as for SA model. A reason for this is discussed in the next paragraph. Comparison of results (drag graphs in Figures 11 and 12) from use of the two turbulence models, show no or little difference at all points except where the non-linearity of the convectional model between 5° and 15° angle of attack using $k-\omega$ not as pronounced as for SA model. This means both turbulence models can predict drag very well for flows over both airfoils.

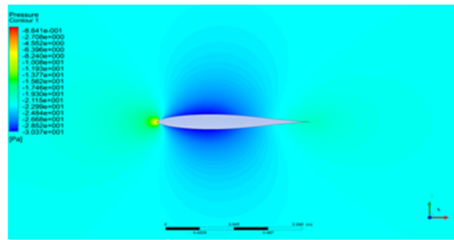
Figure 12: Drag coefficients versus angle of attack using k- ω model

3.5. Pressure Contours

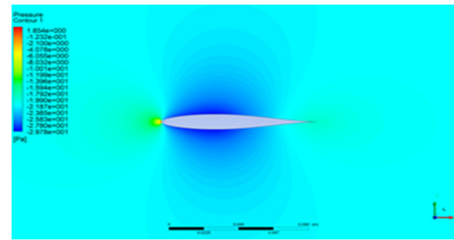
Generally, high pressure region exists at the lower surface of the airfoil and the low pressure region is on top of it. Due to the pressure difference, the flow from the bottom surface to the top surface at the trailing edge creates a low-pressure region (Kunya, 2019). This low pressure region is much lower than the pressure on the top surface, which creates favorable pressure gradient in the front part but an adverse pressure gradient in the rear part, as shown below. This adverse pressure gradient slows down the velocities inside the boundary layer which causes the recirculation region close to the top surface of airfoil. This recirculation region continues to grow upstream as more air is accelerated from bottom to top surface of airfoil. Figure 13a to 13h shows the contours of pressure from the SA model for bumpy and conventional airfoils. Figures 13a and 13b show pressure contours at 0° angle of attack for bumpy and conventional airfoil. The blue colour indicates lower pressure, and pressure at airfoil bottom surface is the same as that of top surface, hence there is no lift. As the angle of attack is increase from 0° (Figures 13c to 13h), airfoils bottom pressure becomes greater than the top surface pressure as indicated by the colours of the contour, and the difference in pressure between the two surfaces is proportional to angle of attack. The lift value increases as the pressure difference increases. Same thing is said about NASA airfoil by Isyaku (2019).

3.5.1. Velocity contours

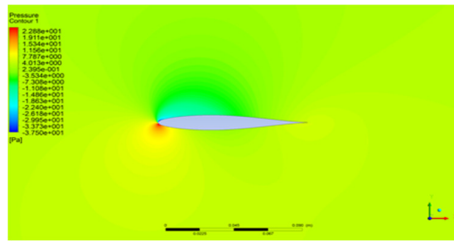
Flow over the airfoil boundaries was intact from the angle of 0° to 5° , as there was no flow separation and the lift curves were aligned for both conventional and bumpy airfoils. At 5° , flow separation starts for both airfoils and continue at higher angles, with the effects of drag becoming dominant and the airfoil entering stall conditions (Isyaku, 2019). Figures 14a to 14h show the velocity contours. The contours of velocity at 15° and 20° angle of attack for the conventional and bumpy airfoils are compared as shown by the Figures 14e to 14h. Flow separation was delayed for the airfoils with bumps. The results revealed that bumps along the leading edge produced stream-wise vortices. These vortices carried higher momentum flow in the boundary layer, which kept the flow attached to the surface of the airfoil and, in turn delayed separation, and thus enables a higher lift coefficient during post stall (Kunya, 2019).



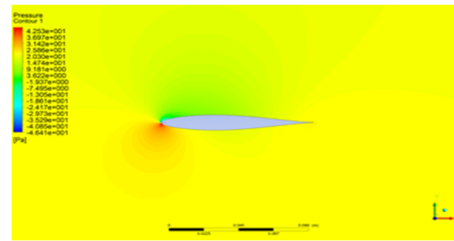
(a): Pressure contours for convectional airfoil at 0°



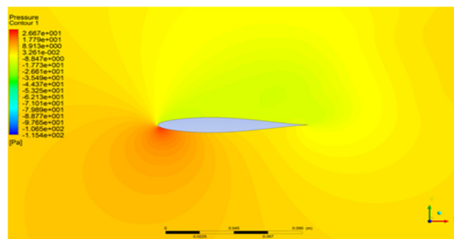
(b): Pressure contours for bumpy airfoil at 0°



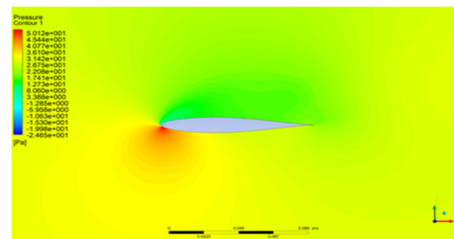
(c): Pressure contours for convectional airfoil at 5°



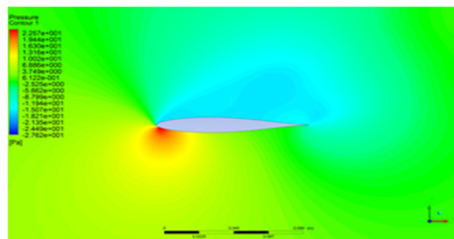
(d): Pressure contours for bumpy airfoil at 5°



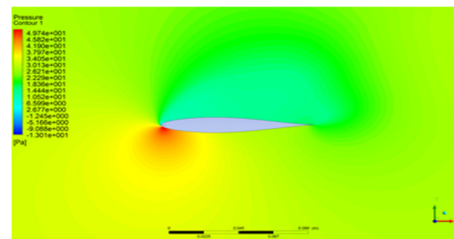
(e): Pressure contours for convectional airfoil at 15°



(f): Pressure contours for bumpy airfoil at 15°



(g): Pressure contours for convectional airfoil at 20°



(h): Pressure contours for bumpy airfoil at 20°

Figure 13: Pressure contours

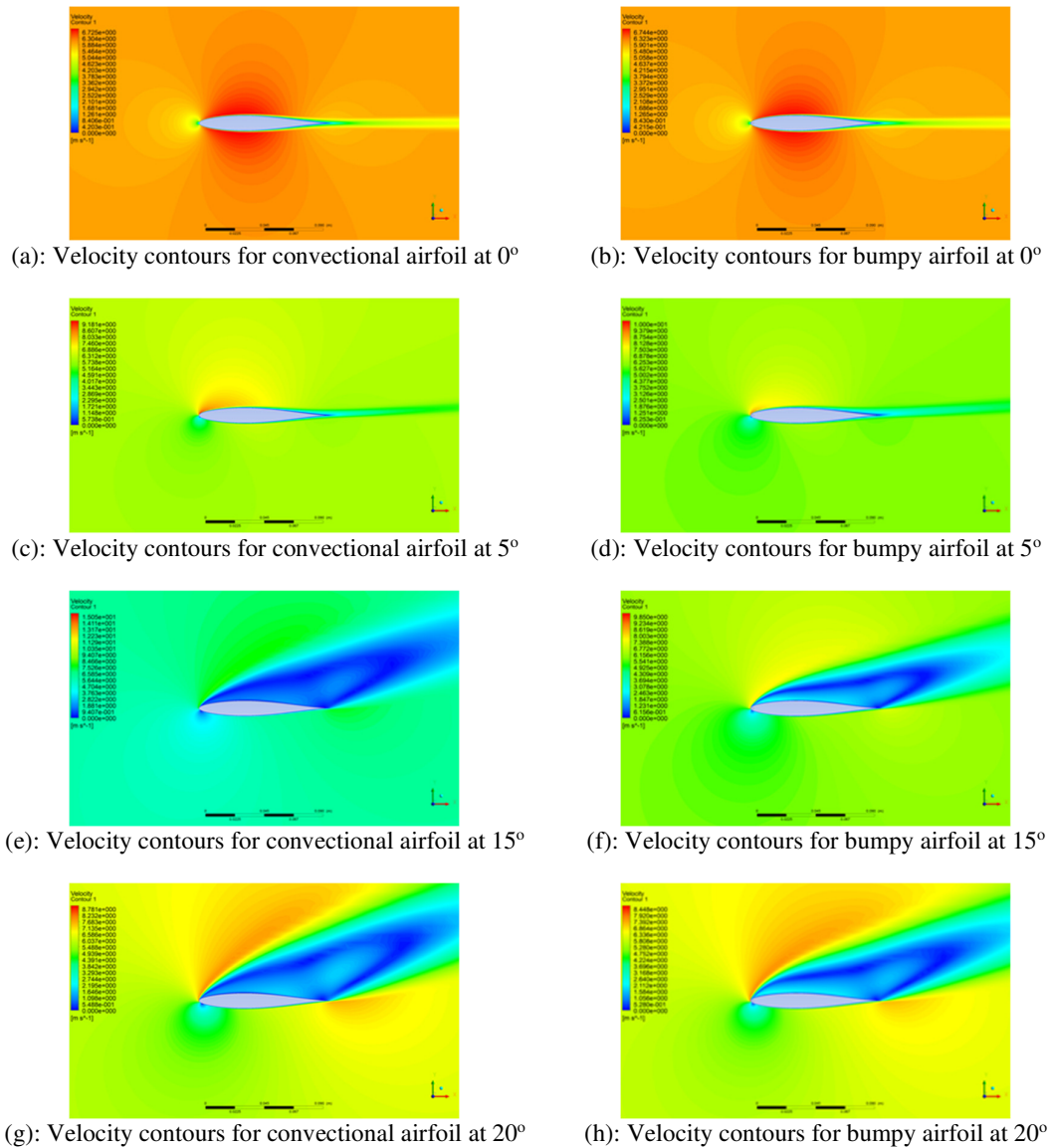


Figure 14: Velocity contours

4. CONCLUSION

The bumpy airfoils showed increased maximum lift coefficient and a larger stall angle than the conventional airfoil. This is due to the fact that bumps along the leading edge produced stream-wise vortices. These vortices carried higher momentum flow in the boundary layer, which kept the flow attached to the surface of the airfoil and, in turn delayed separation, and thus enables a higher lift coefficient during post stall. Both turbulence models' predictions show almost similar results with regard to lift and drag values.

5. ACKNOWLEDGMENT

The authors wish to acknowledge the assistance and contributions of Abdullahi Dada of the Department of Mechanical Engineering, Ahmadu Bello University, Zaria, Nigeria for the computer resource.

6. CONFLICT OF INTEREST

There is no conflict of interest associated with this work.

REFERENCES

- Anil, K. M. (2007). Numerical Analysis of Effects of Leading-Edge Protuberances on Aircraft wing Performance. Master's Thesis, Department of Aerospace Engineering, Faculty of Graduate School, Wichita State University.
- Carija, Z., Marusic, E., Novac, Z. and Fucak, S. (2014). Numerical Analysis of Aerodynamic Characteristics of a Bumped Leading Edge Turbine Blade. *Engineering Review*, 34(2), pp. 93-101.
- Douglas, J. F., Gasiorek, J.M., Swaffield, J. A. and Jack, L. B. (2005). *Fluid Mechanics*. 5 Ed., Dorling Kindersley (India) Pvt. Ltd., pp. 452-462.
- Dylan Walsh (10320467) Energy Systems Engineering (2013). 50 kW Horizontal Axis Wind Turbine. NUI Galway 3rd Year Energy Systems Project.
- Fish, F. E. and Battle, J. M. (1995). Hydrodynamic Design of the Humpback Whale Flipper. *Journal of Morphology*, 225, pp. 51-60.
- FLUENT 6.3 (2006). Introductory Notes. Fluent User Services Centre. www.fluentusers.com
- GAMBIT 2.3. (2006). Introductory Notes", Fluent User Services Centre. www.fluentusers.com
- Gawad, A. F. A. (2012). Numerical Simulation of the Effect of Leading-Edge Tubercles on the Flow Characteristics around an Airfoil. In: *Proceedings of the ASME 2012 International Mechanical Engineering Congress & Exposition IMECE2012-85857, Houston, Texas, USA*.
- Hansen, K. L., Kelso, R. M. and Dally, B. B. (2011). Performance Variations of Leading Edge Tubercles for Distinct Airfoil Profiles. *AIAA Journal*, 49(1), pp. 185-194
- Isyaku, B. K. (2019). Simulation and Experimental Investigation of the Performance of a Developed Whale-Inspired Wind Turbine Blade at Low Wind Speed. PhD Thesis, Ahmadu Bello University, Zaria, Nigeria.
- Kunya, B. I., Folayan, C. O., Pam, G. Y., Anafi, F. O. and Muhammad, N. M. (2019). Experimental and Numerical Study of the Effect of Varying Sinusoidal Bumps Height at the Leading Edge of the NASA LS (1)-0413 Airfoil at Low Reynolds Number. *CFD Letters*, 11(3), pp. 129-144.
- Asli, M., Gholamali, B. M. and Tousi, A. M. (2015). Numerical analysis of wind turbine airfoil aerodynamic performance with leading edge bump. *Mathematical Problems in Engineering*, 2015.
- Miklosovic, D. S., Murray, M. M. and Howle, L.E. (2007). Experimental Evaluation of Sinusoidal Leading Edge. *Journal of Aircraft*, 44(4), pp. 1404-1407.
- Nasser, A. and Javad, M. (2012). An Introduction to Computational Fluid Dynamics. Chapter 20 in Fluid Flow Handbook. Department of Mechanical and Industrial Engineering. University of Toronto. www.ewp.edu/hartford/~ernesto/F2012...
- Thumthae, C. and Chitsomboon, T. (2009). Optimal Angle of Attack for Untwisted Blade Wind Turbine. *Renewable Energy*, 34, pp. 1279-1284.